



PCCP

Three-Dimensional Line Edge Roughness in Pre-and Post-Dry Etch Line and Space Patterns of Block Copolymer Lithography

Journal:	<i>Physical Chemistry Chemical Physics</i>
Manuscript ID	CP-ART-10-2019-005398.R1
Article Type:	Paper
Date Submitted by the Author:	25-Nov-2019
Complete List of Authors:	Pinge, Shubham; Cornell University Qiu, Yufeng; Cornell University Monreal, Victor; EMD Performance Materials Baskaran, Durairaj; EMD Performance Materials Ravirajan, Abhaiguru; Cornell University Joo, Yong Lak; Cornell University

SCHOLARONE™
Manuscripts

Three-Dimensional Line Edge Roughness in Pre-and Post- Dry Etch Line and Space Patterns of Block Copolymer Lithography

Shubham Pinge¹, Yufeng Qiu¹, Victor Monreal², Durairaj Baskaran², Abhaiguru Ravirajan¹ and Yong Lak Joo^{1,*}

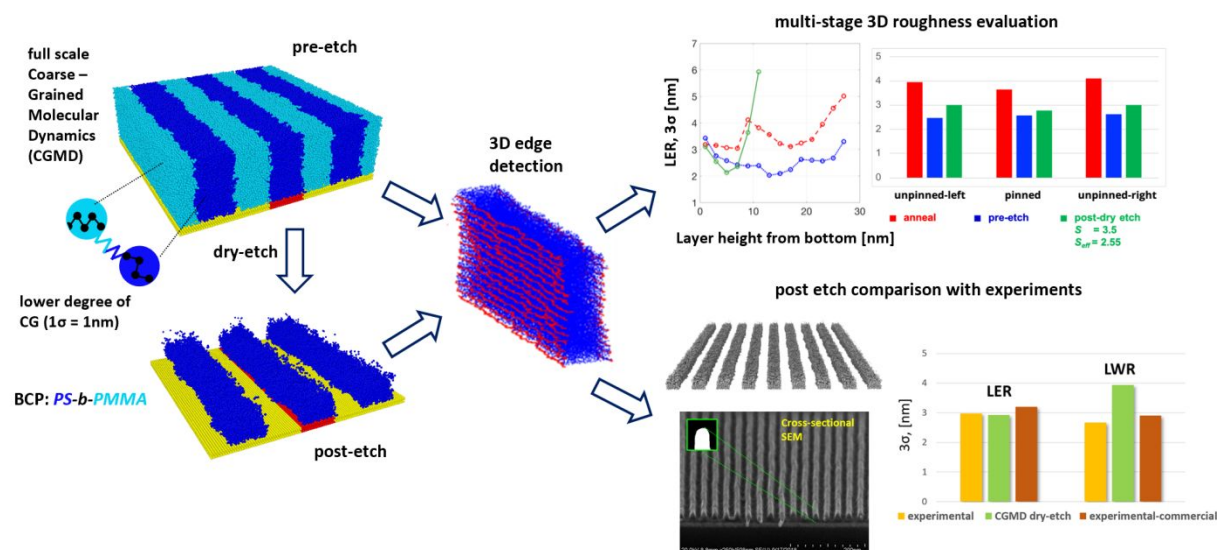
1. Robert Frederick Smith School of Chemical and Biomolecular Engineering, Cornell University, Ithaca, NY 14853 (USA)

2. EMD Performance Materials Corp., 70 Meister Avenue, Somerville, NJ 08876, USA

*E-mail: ylj2@cornell.edu

Abstract: In this work, we employ large-scale coarse-grained molecular dynamics (CGMD) simulations to study the three-dimensional line edge roughness associated with line and space patterns of chemo-epitaxially directed symmetric di-block copolymers (BCPs) on a flat substrate. The diblock copolymer chain length and interaction parameters are validated with experimental BCP period, L_0 and corresponding molecular weight. Defect-free lamellae are formed, after which the system is quenched below the glass transition temperature before selectively dry-etching off one of the BCP phases. The effect of varying etch-selectivity on post-etch resist domain morphology were studied. The roughness of the polymer domain was evaluated over three process stages: anneal, pre-etch, and post-etch. Power spectral density plots were then generated to elucidate the contribution of low and high frequency roughness for the three process stages. The roughness results obtained from simulations is shown to be in close agreement with roughness from analyzing experimental SEM images. Parameters like the Hertz roughness exponent and correlation length inherent to the process and the BCP were also revealed from the experimental study.

Keywords: block copolymer lithography; directed self-assembly; dry-etching; roughness analysis



I. Introduction

Over the past decade, with the ever-increasing demand for miniaturization of micro-electronic devices, directed self-assembly (DSA) of block copolymers (BCPs) has attracted the interest of both academia and industry to develop optimal, defect free nanolithographic patterns due to its low-cost. Also, it is not restricted by inherent diffraction-based limitation.¹⁻⁵ The periodic spatial arrangement of the micro-phase separated bulk BCP⁶ is seldom perfectly achieved without it being directed. In the semi-conductor industry, two of the popular techniques are used include graphoepitaxy⁷⁻⁹, which uses surface features and confinement to direct the BCP and chemoepitaxy^{3, 10-13}, which uses enthalpic interactions via chemical patterning to control the BCP ordering. Compared with chemoepitaxy, graphoepitaxy is harder to perform on a large scale to get lamellae structure, it is more often used to get ordered cylindrical domains or smaller scale lamellae structure. Among chemoepitaxial technologies to form line space patterns, Liu-Nealey (LiNe) flow with near symmetric polystyrene-*block*-polymethyl methacrylate (PS-*b*-PMMA) has been widely considered as a prospective DSA candidate for commercialization.¹²⁻¹³ The PS-pinned region is patterned with cross-linked PS mat film while the rest of the substrate is grafted by random hydroxyl terminated PS-*co*-PMMA chains (neutral layer) usually of a lower chain length than the PS mat. PS-*b*-PMMA BCP is then spin coated on top of this chemically patterned substrate and annealed at elevated temperatures (250-300°C) to obtain defect-free BCP lamellae.

Once this ideal lamella morphology is formed, PMMA is selectively removed, forming a nanolithographic pattern template of the remaining PS domain. This exercise leaves the patterned substrate exposed and can be further processed for semiconductor applications. The etching process can either be performed with a selective solvent like acetic acid (wet-etching) or using a variety of plasma etches(dry-etching) such as O₂ / Ar.¹⁴⁻¹⁷ While wet-etching is more selective than dry-etching, it has a tendency for the pattern to collapse especially for high BCP film thicknesses and low solvent conditions due to the diverging surface forces during solvent evaporation. Therefore, even though dry-etching has substantially lower selectivity, using plasma ions has been preferred over the more economical wet-etching for line and space patterns.

In dry-etching, a lower ion to radical ratio leads to rougher surfaces. Ion bombardment removes PMMA by striking the material with high energy etch ions forming volatile products like CO and CO₂. These volatile products are enhanced by the presence of Ar ions which break bonds on the surface and depolymerizes PMMA, leading to high etch rates¹⁸⁻²⁰. This removal of materials also

causes the formation of dangling bonds which have the ability to recombine with newly exposed surface or residual material, forming a cross-linked polymer mini-network and increasing the etch-resistance to subsequent ion-bombardment. This tendency to cross-link is higher for PS than PMMA and plays a crucial role in affecting the surface morphology of the etched material²⁰⁻²⁴. On the other hand, oxygen radical reacts with the oxygen groups to chemically remove PMMA. These radicals are often known to form passive inhibition layer as a byproduct. The presence of Ar ion in addition to O₂ radicals help in removal of this inhibition layer²⁴, and as a result, increase the PMMA removing rate.

The anisotropic imperfections caused by the etching process coupled with the inherent BCP interfacial width leads to line-edge roughness (LER) and line-width roughness (LWR) in the line and space patterns. LER is defined as the 3σ deviation of a line-edge from the mean straight line. High LER values in the features leads to hindrance in the flow of electrons leading to anomalies in the device resistance and capacitances making the device inviable.²⁵⁻²⁶ The 2015 International Technology Roadmap for Semiconductors has listed DSA among one of the top prospective next-generation lithographic alternatives, but the current high 3σ LER values need further improvements for its commercialization²⁷. To achieve this goal, it is important to characterize and quantify the roughness along the film thickness as opposed to the approximated top-down values obtained from SEM images.

Modeling and simulations can aid the manufacturer in this regard. A wide range of DSA modeling work has been achieved using a Self-Consistent Field (SCF) or Theoretically Informed Coarse-Grained (TICG) framework²⁸⁻²⁹. While SCFT has been prevalently used over the years to predict the theoretical BCP phase diagrams, interfacial width cannot be accurately measured if the fluctuations are not accounted for. TICG with its improvised strategies considers fluctuations and has been popularly used in recent years to study chemoepitaxial DSA, especially to predict the energetics of defect annihilation.³⁰⁻³¹ Owing to the higher degree of coarse-graining, the roughness values computed using TICG or allied methodology like Single-Chain-in-Mean-Field (SCMF) simulations is limited to low frequency estimation in the frequency domain. Dauloas and co-authors have studied the effect of roughness of the patterned substrate and its propagation through the film thickness, for undulated and peristaltic low frequency variation using a SCMF approach with successful comparison with experiments.³²⁻³³ Recently, Segal-Peretz *et al.* have demonstrated the implementation of TICG in conjunction with scanning transmission electron microscopy to

characterize the three-dimensional structure of DSA with high- χ BCP, P2VP-*b*-PS-*b*-P2VP.³⁴ Coarse-grained polymer field-theoretic simulations have also been employed by Bosse and co-authors to predict the interfacial fluctuations for BCP resists with a peak in the spectral plots at the BCP interdomain spacing.²⁷ Although these simulations are computationally economical, the authors categorically state their limitations in characterizing high frequency roughness and suggest the need for intensive particle based molecular dynamics (MD) approach for a more complete understanding. Among the few available MD literature on the subject, there is a lack of matching of the BCP chain length to the actual molecular weight and the corresponding experimental BCP pitch (L_0^{exp}).³⁵⁻³⁶ More importantly, none of the above stated works study the resist morphology evaluation after etching one of the BCP phases. While characterizing the interfacial deviations is crucial, the actual pattern transfer to the underlying silicon substrate takes place with the removal of the non-resist BCP phase.

In this work, we have used large-scale coarse-grained molecular dynamics (CGMD) simulations with close matching of experimental and simulation BCP molecular weights, and substrate dimensions to study the 3-dimensional BCP morphologies of DSA with LiNe flow over three process stages: after annealing, after quenching below glass transition of BCP (pre-etch), and after selective dry-etching of the PMMA phase (post-etch).

II. Models and methods

Simulation system overview

A flat, patterned substrate was used for the LiNe flow simulations. The patterned part of the substrate is selective to PS while the unpatterned part is neutral. The selectively patterned substrate that corresponds to the cross-linked PS mat (red part in figure 1a) has a pinning width (pw) = 16 nm ($\sim 0.57 L_0$) and a density multiplication of $3X$, indicating 3 domains each of PS and PMMA per patterning. The non-patterned part of the substrate (yellow part in figure 1a) that mimics the neutral brush in experiments is non-selective towards either of the phase. Figure 1b shows the post-anneal BCP morphology profiles.

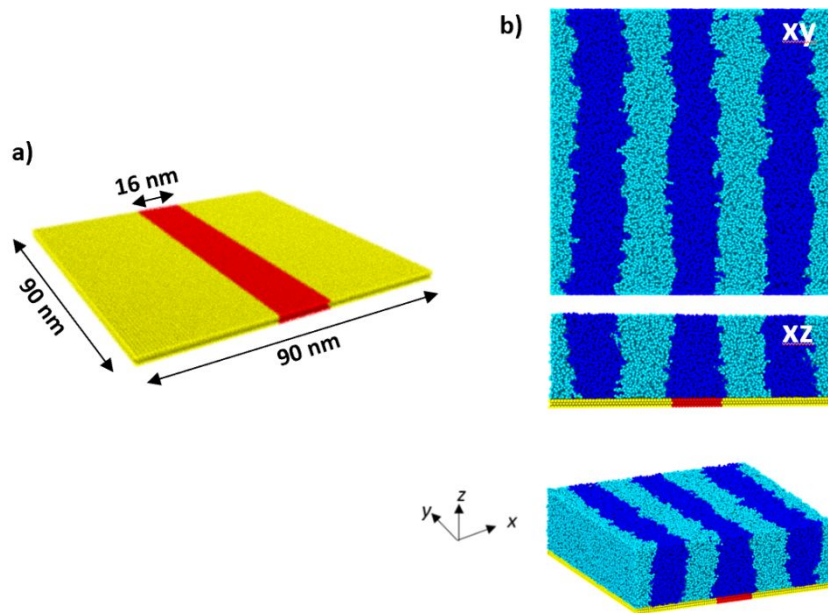


Figure 1. a) CGMD simulations flat substrate, b) morphology profile after annealing ($T_{\text{anneal}}=1.2$). PS mat shown in red, neutral brush in yellow, PS domain in blue, PMMA domain in cyan.

On the top of BCP domain, there is a neutral top layer (not shown in figure 1) to prevent BCP beads from escaping the simulation box from the z direction. This top substrate has the same properties and interaction parameters as the neutral part of the bottom substrate.

Simulation system parameters

The polymer chain is modeled as an AB block with both monomer radii (σ') equal to 1 nm. In block A , each bead contains 4 monomers of PS while in block B , each bead contains 4.5 monomers of PMMA to account for the difference in bulk densities of the two monomers. Each polymer chain comprises of 63 beads of PS ($\sim 26,000 \text{ g mol}^{-1}$) and 58 beads of PMMA ($\sim 26,000 \text{ g mol}^{-1}$). The reduced mass of each bead is adjusted according to the respective coarsening for PS and PMMA. The interaction between bonded BCP beads is given by the fene bond potential in equation 1, where $K=30 \epsilon \sigma'^{-2}$ is the spring constant of the BCP bond while $R_{\text{max}} = 1.5\sigma'$ is the maximum bond extensibility.³⁸

$$U_{\text{fene}}(r) = -0.5KR_{\text{max}}^2 \ln[1-(r/R_{\text{max}})^2] \quad (1)$$

The favorable long-range interactions are governed by a tail-corrected Lenard Jones interaction⁹ given by equation 2 while the repulsive interaction is in accordance to Weeks-Chandler-Anderson³⁹ (WCA) potential as equation 3.

$$U_{\text{attractive}}(r) = 4\epsilon[(\sigma'/r)^{12} - (\sigma'/r)^6] + S_{\perp}(r) \text{ for } r < 2.5 \sigma' \quad (2)$$

$$U_{\text{repulsive}}(r) = 4\epsilon[(\sigma'/r)^{12} - (\sigma'/r)^6] + \epsilon \text{ for } r < 2^{1/6} \sigma'.^{44} \quad (3)$$

A global BCP site density of 0.85 beads nm⁻³ is maintained and the thermostat employed is Nosé-Hoover. The BCP in the study corresponds to PS-*b*-PMMA with $L_0^{\text{exp}} = 28$ nm. Bulk trials were performed varying the Lenard Jones interaction parameters $\epsilon_{\text{BCP-BCP}}$ to elucidate parameters for $L_0^{\text{sim}} \sim L_0^{\text{exp}}$ for various chain lengths. The optimized parameters from the bulk study, $\epsilon_{\text{PS-PS, attractive}} = 0.15$, $\epsilon_{\text{PMMA-PMMA, attractive}} = 0.15$, and $\epsilon_{\text{PS-PMMA, repulsive}} = 0.15$ were used for the main simulations. The simulation box is periodic in x and y and fixed in z with a BCP film thickness same as $L_0 = 28$ nm. The substrate is three layered thick ($3\sigma'$) with hexagonal packing. As the maximum cut-off radii for any interaction is $2.5\sigma'$, any thickness greater than $2.5\sigma'$ will not affect the BCP morphology. The neutral substrate beads interact with the BCP with $U_{\text{attractive}}(r)$. The pinned substrate interacts with PS beads by $U_{\text{attractive}}(r)$ and with PMMA beads by $U_{\text{repulsive}}(r)$. The default interaction strength of the neutral brush and pinned area with the BCP, $\epsilon_{\text{BCP-neutral}} = 0.15$, $\epsilon_{\text{PS-pinned, attractive}} = 0.15$, $\epsilon_{\text{PMMA-pinned, repulsive}} = 0.15$.

Independent bulk trials were performed with only the PS part of the BCP (N_{63}) and the mean squared displacement of the equilibrated melt was plotted for temperatures ranging from 0.1 to 1.2.⁴² The point of change in slope of the curve thus generated denoted the glass transition temperature $T_g \sim 0.3$.

Different simulation stages

In the first stage of the process, the system is annealed at $T_{\text{anneal}} = 1.2$ to form defect free lamellae. Since this temperature is substantially higher than the glass transition temperature, similar to the experimental temperature range, it can be used to represent the experimental annealing temperature. This simulation temperature is just below the critical temperature beyond which it gets difficult for the simulation setup to track the BCP beads owing to the high kinetic energy leading to possible loss of beads. Annealing at lower temperatures would require longer anneal times to form lamellae, further increasing the associated computational expense. It is also

important to note that true experimental time (~tens of mins) is not achieved in MD simulations at these length-scales, but we seek to maintain the relative time scales at different process stages. The post-anneal lamellae morphology profile formed is shown in figure 1b. With the suitable LJ interaction strength illustrated, the defect free structures form in ~ 7 million steps with a timestep = 0.01τ (τ being the reduced time). The structures were then cooled to $T_{etch} = 0.15$, below T_g of PS in the second process stage.

After the system is equilibrated below T_g , the morphology is served as the starting trajectory which is etched via a simulated ion-bombardment mechanism in the third process stage. For model simplicity, the etch bead is assumed to have a same size of 1 nm as the BCP bead. Future version of this model can have added complexity with specific coarse-graining. Two types of etch beads are defined which can only etch off a BCP domain it is selective to and remain immune to the other.. By varying the number ratio of these two types of etch beads, the selectivity of dry etching can be controlled. Experimentally, the etching selectivity is gained by controlling the etch-gas chemistry. After the pre-etch process stage, the BCP beads are frozen and the top-substrate beads are removed from the simulation box. The box is then rescaled to increase in size in the positive z direction. Subsequently, in the space above the BCP thin film PS and PMMA selective etch beads are generated. These etch beads are provided with a velocity in the z -direction, $V_z = 0.01 \sigma'/\tau$ (σ' is the reduced distance and τ is the reduced time) as they approach the BCP beads. At every 10 timesteps (timestep = 0.01τ), any BCP beads within the etch radii ($R_{etch} = 1.1 \sigma$) of the etch bead center will be removed from the simulation box to simulate ion-bombardment etching. The reason for choosing every 10 timesteps is to decrease the computing resource consumption while also to simulate a sufficiently low reaction time prior to the bead removal. With increasing time, more of the BCP beads are consumed and lower film thicknesses close to the bottom substrate is exposed to the incoming etch beads. The etching process is stopped when all the PMMA phase is consumed resulting in a post-etch PS domains resting on the bottom substrate. Figure 2 illustrates this process.

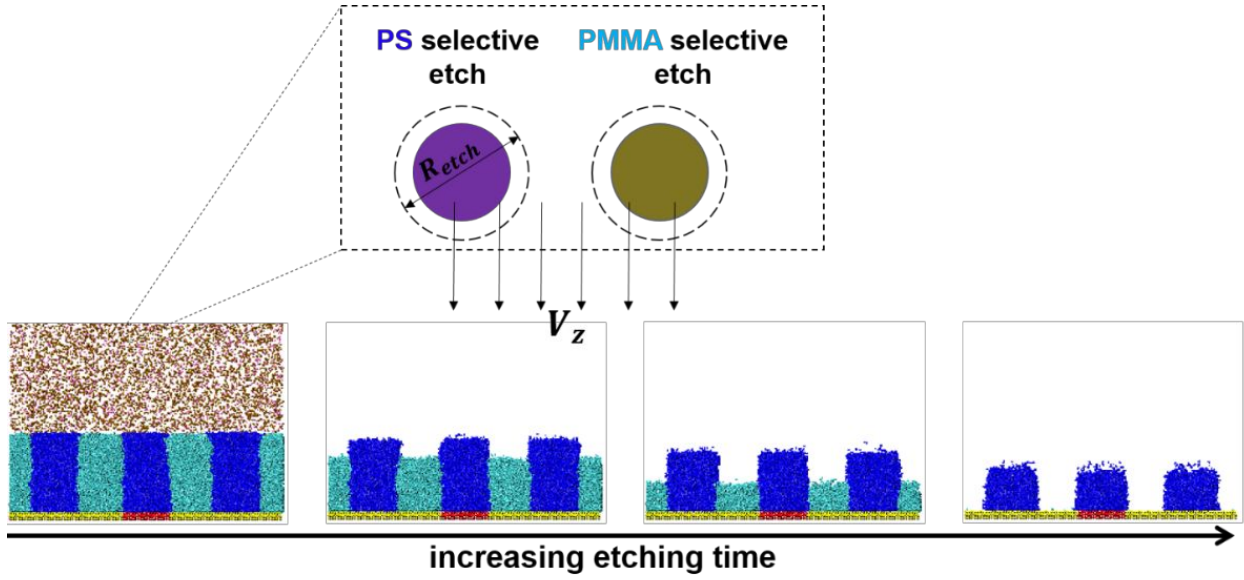


Figure 2. Kinetic evolution of resist morphology with PS selective and PMMA selective etch beads. PS selective beads removes PS beads while PMMA selective beads remove PMMA.

Etch beads possess high energy and move at a near collisionless state with each other. As the pressures in the system are in the range of tens of mTorr, this assumption of collisionless state is fair. For interaction between etch beads, a soft cosine potential with a substantially lower energy prefactor $\varepsilon=0.05$ and a cut off radius $r_c=1.0$ is described as in equation 4. The soft potential essentially prevents any etch bead overlap while maintaining the collective sheath velocity, V_z .

$$E(r) = \varepsilon \left[1 + \cos\left(\frac{\pi r}{r_c}\right) \right] \quad (4)$$

The etching was performed at $P=10$ mTorr to maintain a etch bead density of 0.0165 beads/nm³ (refer SI for etch beads coarse-graining). Etching selectivity is the PMMA etching rate over PS etching rate, calculated via equation 5. $r_{\text{etch-PMMA}}$ is the PMMA etching rate and $r_{\text{etch-PS}}$ is the PS etching rate, $N_{\text{PMMA-selective etch}}$ is the number of PMMA selective etching beads, $N_{\text{PS-selective etch}}$ is the number of PS selective etching beads. It depends on parameters like etch-chemistry, bias voltage source among others. Choosing the appropriate etch-gas with the optimum selectivity requires a thorough investigation of the etching mechanics and post-etch chemistry which is out of this study's scope. Selectivities 1.5, 2, 2.5, 3.5 were applied in this paper.

$$\text{selectivity } (S) = \frac{r_{\text{etch-PMMA}}}{r_{\text{etch-PS}}} = \frac{N_{\text{PMMA-selective etch}}}{N_{\text{PS-selective etch}}} \quad (5)$$

The post-etch morphology is then evaluated for its effective selectivity, resist height, line-width roughness and line-edge roughness in space and frequency domains.

Experimental verification

The experimental trials were performed with the LiNe flow process using the block copolymer, PME-7001 on NLD-128 (PS mat pinning) and NLD-127 (neutral brush) prepattern. The pattern multiplication is $3X$ with a patterning pitch of 90 nm and a pinning width of 18 nm (optimum for experimental trials). The film thickness is about $1.2L_0 \sim 35$ nm to offer higher tolerance for pattern for post PMMA-etch pattern transfer. Substrate fabrication and annealing conditions have been kept similar to Liu *et al.*¹²⁻¹³ The PMMA phase is etched with Ar/O₂ plasma etch with effective selectivity close to 2.5.

The PS beads coordinates were analyzed at post-annealing, pre-etching and post-etching stages to obtain each PS domain width, LER and LWR. The lamellae BCP was sliced into 2nm thick layers along the film thickness. For each layer, the edges of the domains were located. The distance between the corresponding edges is the width of that domain, and three times the standard deviation of this width is the associated line-width roughness of this domain. Similarly, three times the standard deviation of the edge bead coordinates, along a mean straight line for the layer is the line-edge roughness at that layer height.

Wet-etching was also investigated in this work. Due to its lack of practical relevance, the results are addressed in the supplemental information.

III. Results and discussion

Effect of selectivity on post-etch PS domain morphology

As we define the simulation selectivity parameter as the ratio of number of PMMA-selective etch beads to PS-selective beads, it is important to find the effective selectivity by measuring the post-etch resist heights after complete PMMA removal. As the film thickness is 28 nm, the effective selectivity can be defined as:

$$S_{eff} = \frac{28 - ht_{PMMA}}{28 - ht_{PS}} \quad (6)$$

Ht_{PMMA} and ht_{PS} are the heights of the two domains at any particular time. The kinetic evolution of the system morphology and the effective selectivity for the morphology for three different selectivities is shown in figure 3.

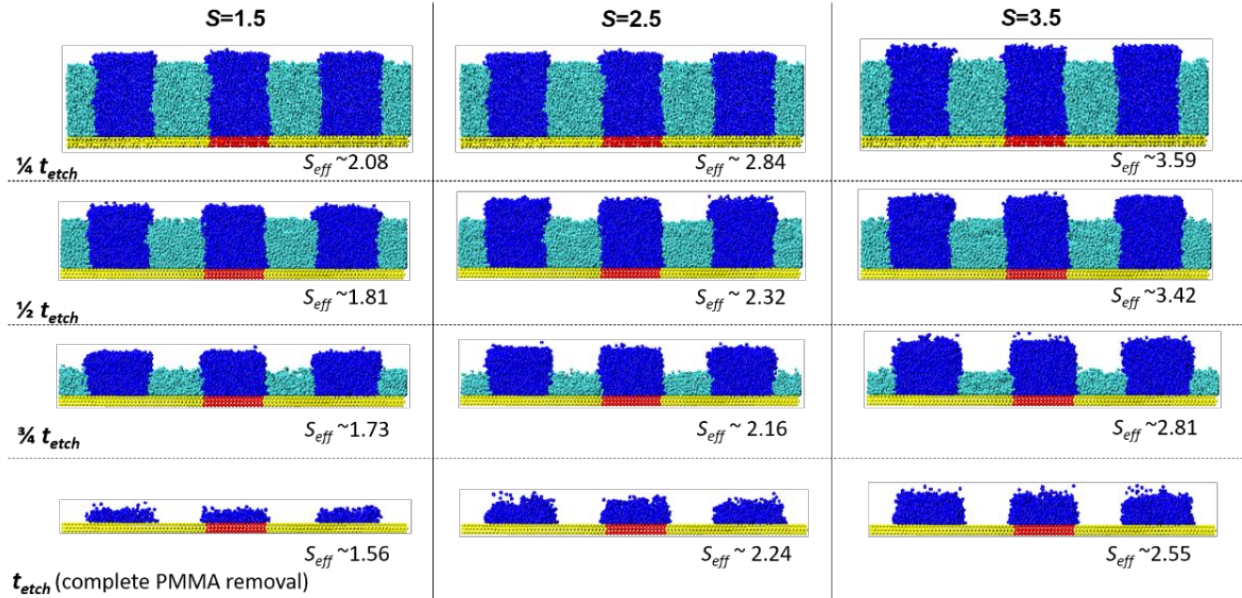


Figure 3. Kinetic evolution of resist profile at constant $P = 10\text{mTorr}$ and $V_z = 0.01 \sigma/\tau$ at three different selectivity, $S = 1.5, 2.5,$ and 3.5 . The effective selectivity is calculated by measuring the PS and PMMA domain heights.

For the same domain thickness, higher initial selectivity, S leads to taller final resist heights at complete PMMA removal. This is expected as the system has a greater number of PMMA-selective etch beads at the same pressure as compared to PS-selective etch beads. The final effective selectivity, S_{eff} is lower than initially defined simulation selectivity parameter, S as the ratio of two types of selective etch beads. The instantaneous S_{eff} also decreases with increasing etch time. For lower etch times, $S_{eff} > S$ and as time increases, the effective selectivity falls below initial selectivity for $S = 2.5$ and $S = 3.5$ while remaining incrementally above initial selectivity for $S = 1.5$ (figure 4).

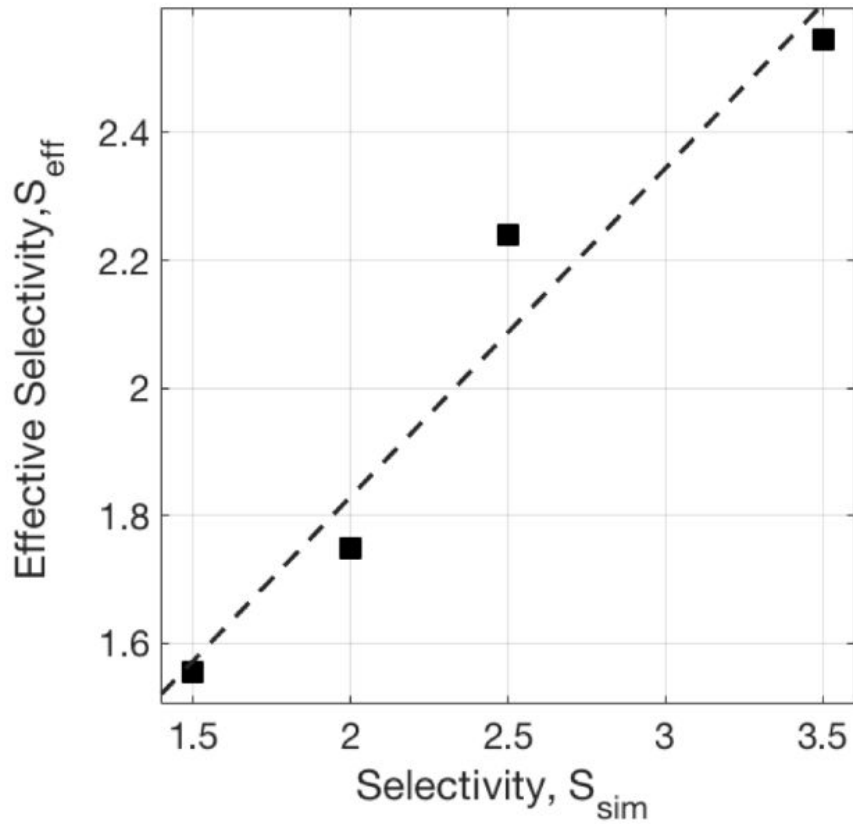


Figure 4. Effective selectivity (S_{eff}) calculated at complete PMMA removal as a function of imposed simulation selectivity (S_{sim})

In the etching process, the post-etch PS domain morphology is evaluated at complete PMMA removal. The Line-Width and the Line-Edge Roughness (figure 5) are plotted as a function of the height measured from the bottom substrate.

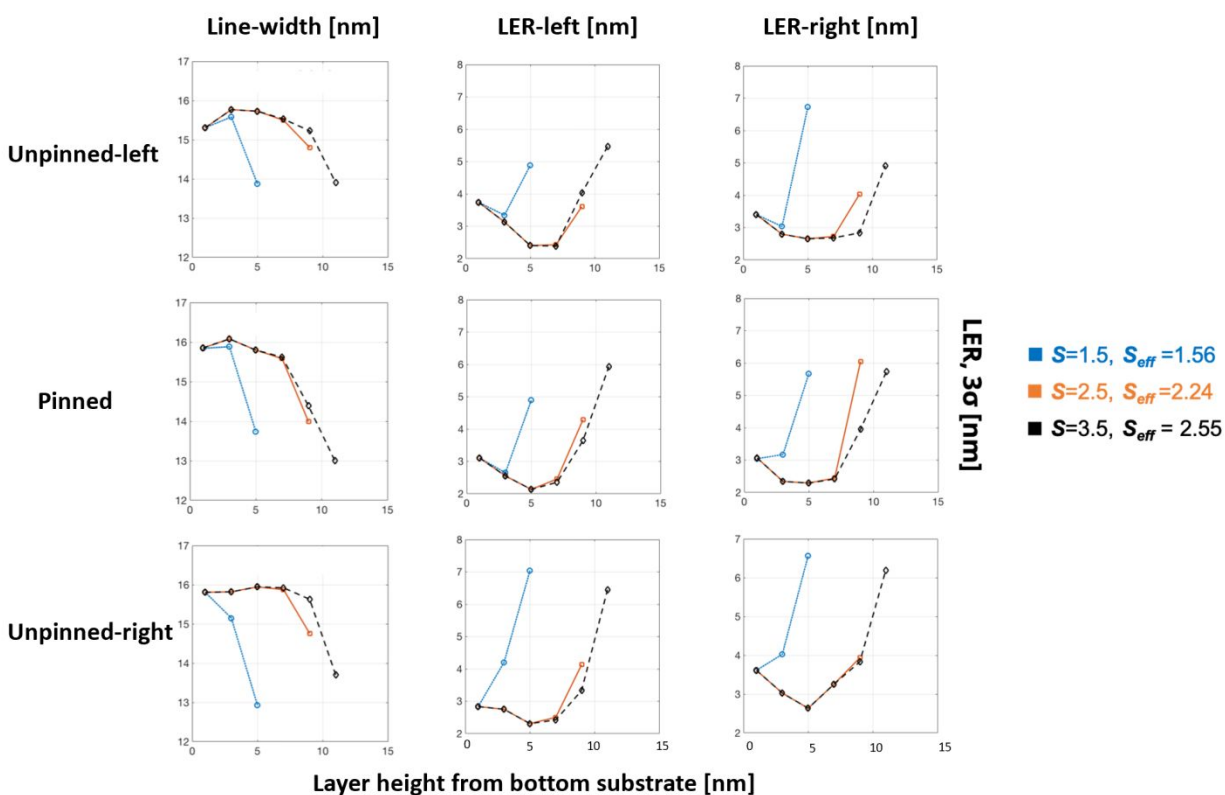


Figure 5. PS Line-Width (left column), PS domains left edge LER (middle column) and PS domains right edge LER (right column) vs. layer height from the substrate plots for three selectivity. Pinned area is the area on the top of cross-linking PS substrate. Unpinned-left is the area at the left of pinned area, unpinned-right is at right.

The results show that away from the bottom substrate, close to PS top surface, the line-width gets lower, leading to a tapered structure in the resist morphology. The tapered top region is also rougher than the edge layers near the bottom surface. This observation is true for all the three selectivities, albeit lower selectivity has lower PS domain heights. It is also important to note that PS domain morphology of the top part which has a lower line-widths will not contribute to the subsequent pattern transfers, but the sidewall roughness below the top PS part will strongly affect the silicon pattern transfer. Thus, for the height averaged LER calculation, the top abrasive substrate is not considered. As $S = 3.5$ leads to a final $S_{eff} = 2.55$, a selectivity reported for the popular Ar/O₂ etch chemistry, we employ $S=3.5$ for subsequent multi-stage LER comparisons.

Multi-stage LER evaluation

The three-dimensional morphology and LER is evaluated along the film thickness and at each stage of the process as shown in figure 6. The PS edge for the post-etch stage has contribution from BCP interfacial width and etching process while pre-etch edges have contribution only from BCP interface fluctuations. For the three PS domains, as evident from figure 6, the height averaged LER is the highest for anneal stage. That is because at the elevated temperatures, as the melt has higher kinetic energy, the interface has higher fluctuations. For the different layers, there is a trend that the layers in the middle have lower LER values comparing with top or bottom parts for all three stages. The effect of the guiding force is more predominant close to the bottom substrate while the upper region of the resist experience lesser effect of the substrate patterning, but bears the highest impact of incoming etch beads. Thus the middle layers show lower roughness values on an average. Cooling the system below glass transition temperature (pre-etch stage) lowers the LER. The sidewall roughness post-dry etch leads to increase in the roughness with a $\langle \text{LER} \rangle = 2.92$ nm, but is still lower than the post-annealing LER. This is in contrast with the post-solvent etch $\langle \text{LER} \rangle$ which is almost same in magnitude with the pre-etch value (refer S.I).

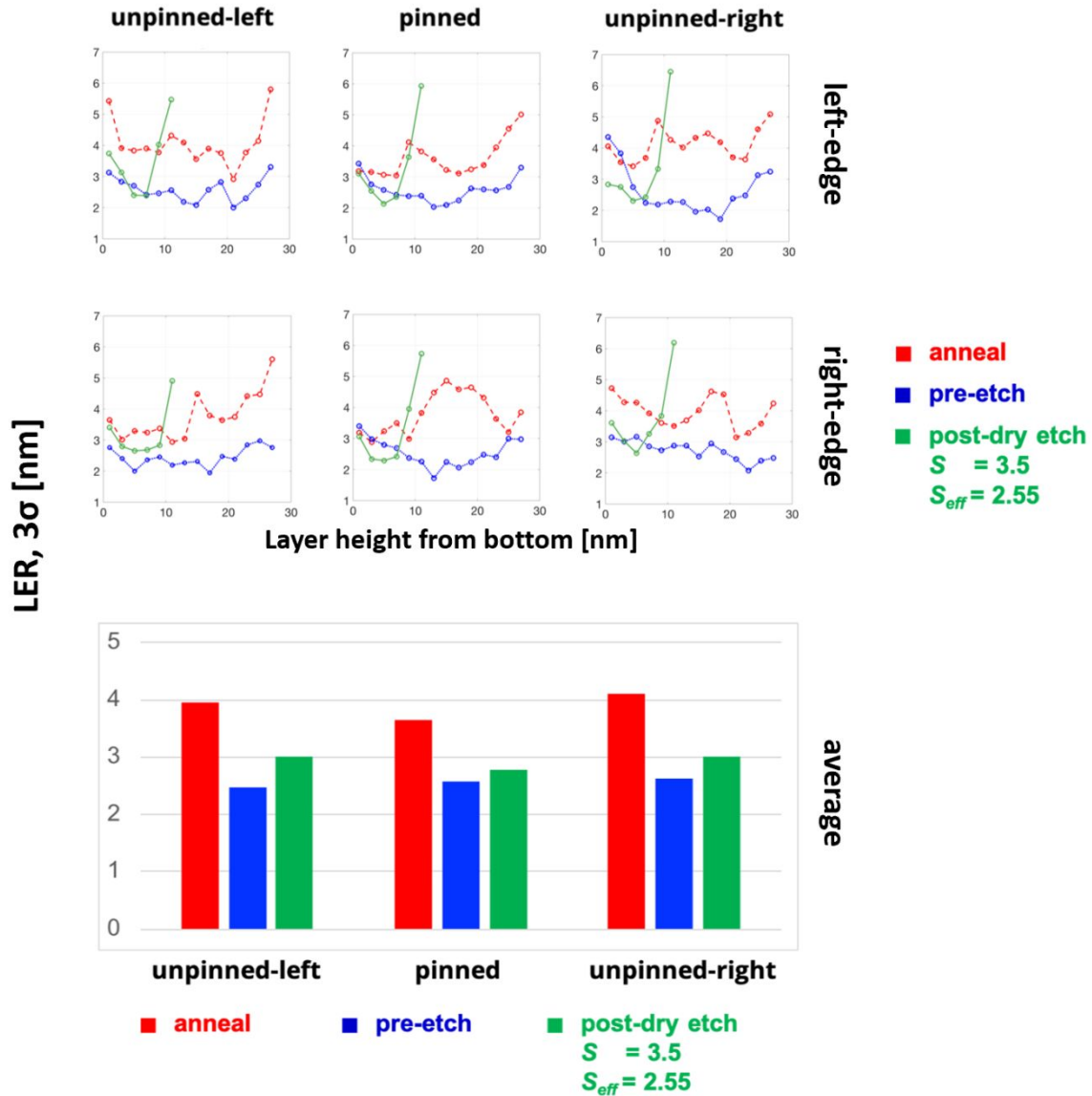


Figure 6. LER vs. film thickness plots (top 2 rows, stand for left edge and right edge respectively) and their average values (third row) for the three process stages: anneal (red), pre-etch (blue) and post-etch (green).

To understand the contributions of the low and high frequency roughness, the power spectral density (PSD) for both edges of the three domains for the planar layers (separated at every 2 nm) were plot as in figure 7. The order followed in the space domain holds true in the frequency domain. On average, $PSD_{anneal} > PSD_{post-etch} > PSD_{pre-etch}$.

For wet-etching simulations, PSD showed higher contribution for low frequencies for post-solvent etch and higher contribution for high frequencies for pre-etch morphologies (refer S.I). This observation is not true for the post-dry etch morphology

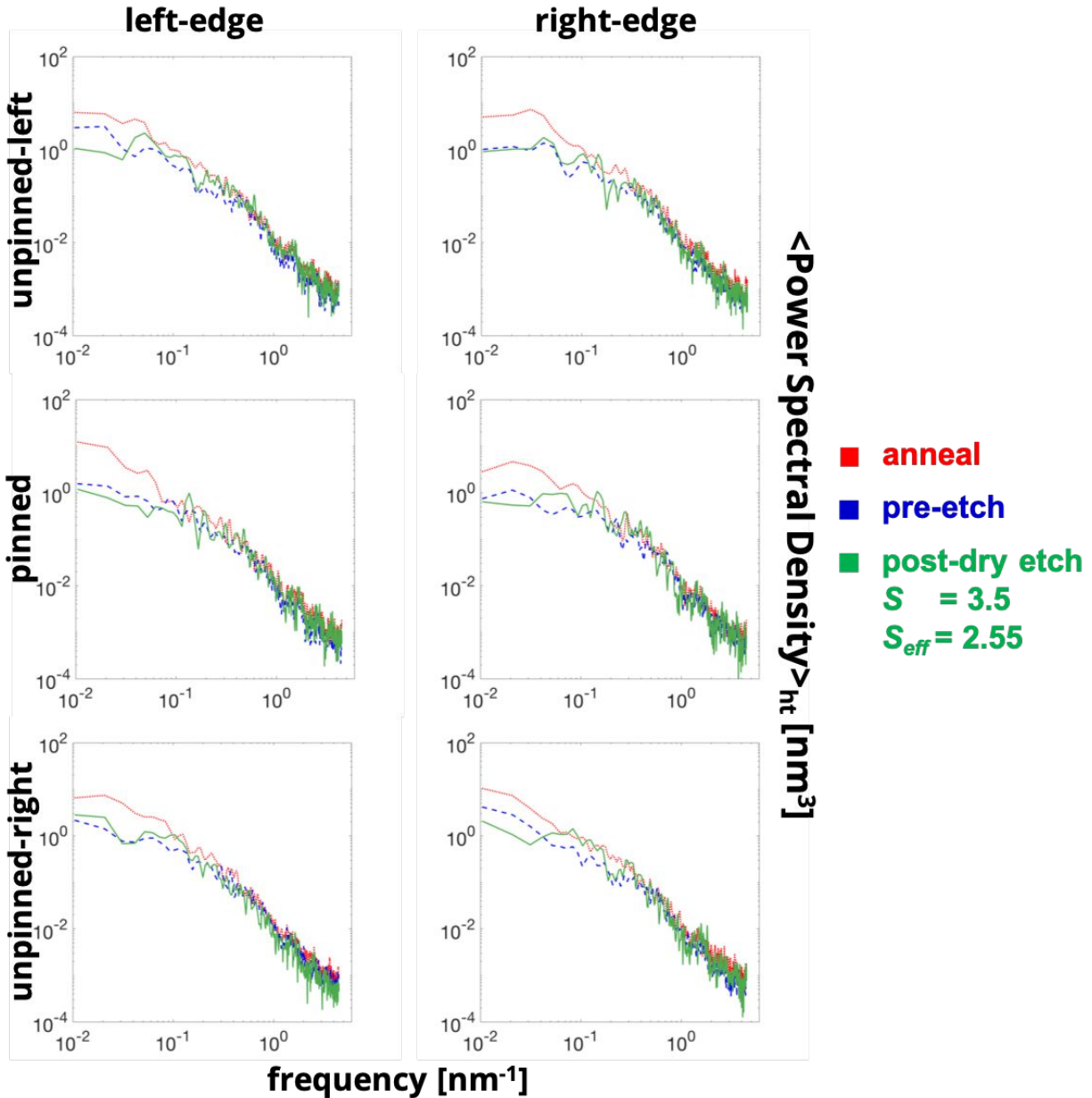


Figure 7. Height averaged power spectral density for PS domains for the three process stages.

Comparison with experimental results

The simulation values are compared to experimental results obtained from a representative SEM image of a self-assembled PS-*b*-PMMA with $L_0 \sim 28$ nm. The PMMA phase of the self-assembled

BCP is etched off with O₂ / Ar based plasma. The experimental SEM image corresponds to a pixel size of ~ 1.25 nm. The image is processed using Median and Gaussian filters after which the edges are detected using a Canny edge detection algorithm (figure 8a).

For the 62 clean lines captured, the $\langle \text{LER} \rangle_{\text{exp}} = 2.98 \pm 0.28$ nm (figure 8b). This is in close agreement with the simulations for the height averaged (every 2 nm) roughness value for the 6 edges, $\langle \text{LER} \rangle_{\text{sim}} = 2.92$ nm. The $\langle \text{LWR} \rangle_{\text{sim}} = 3.94$ nm value predicted from the CGMD simulation show a slight deviation from the SEM image of $\langle \text{LWR} \rangle_{\text{exp}} = 2.67 \pm 0.16$ nm. Although the LWR values are slightly higher, considering the fact that these simulations are coarse-grained with a coarse-graining of 1 nm, under the various assumption of dry-etching, the sufficiently close agreement are encouraging results. To ensure the image analysis method applied here is accurate, roughness was also evaluated using a commercial software, proSEM by Genisys (called experimental-commercial in legend). SEM image is processed using Gaussian filtering and edges were detected using Sigmoidal Fit method. $\langle \text{LER} \rangle_{\text{exp-com}} = 3.20$ nm, $\langle \text{LWR} \rangle_{\text{exp-com}} = 2.90$ nm. Results from two different experimental image analysis methods are in good agreement, validating the image analysis method and the simulation model

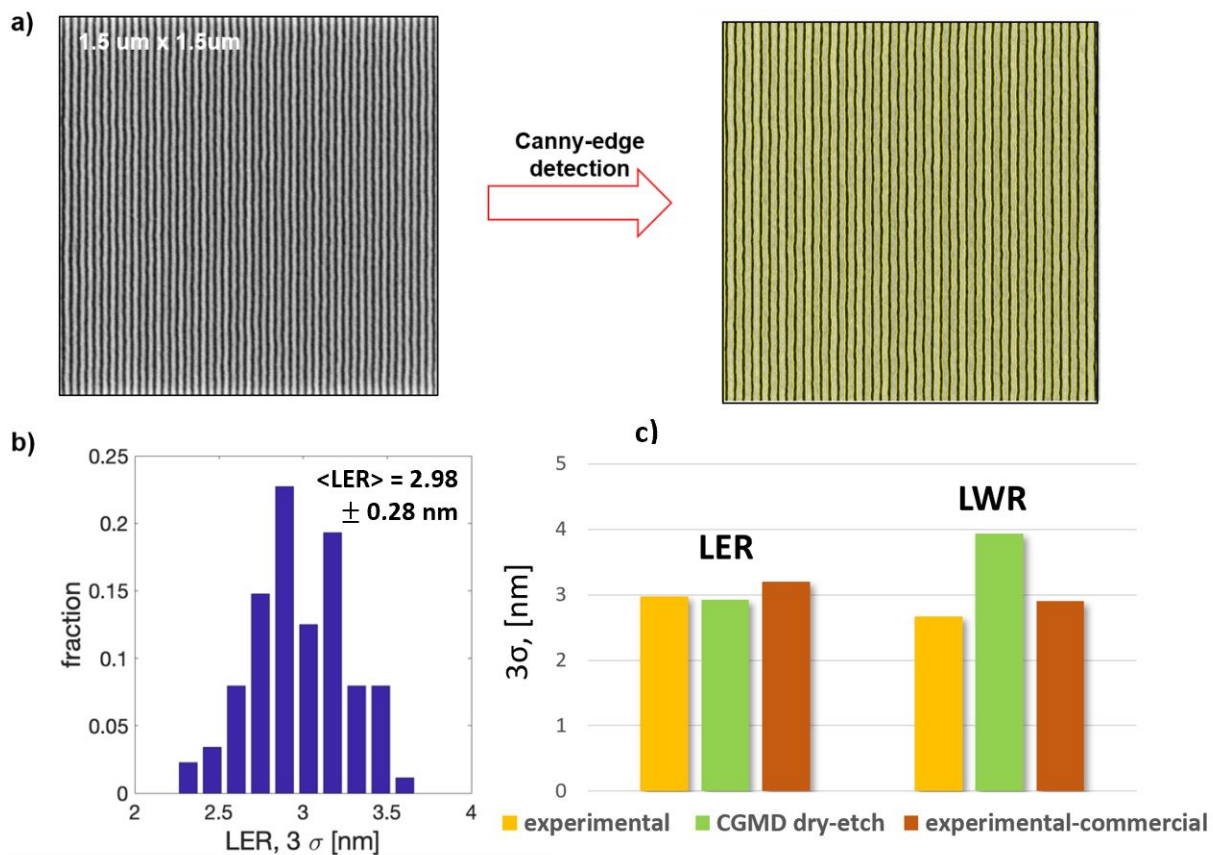


Figure 8. a) Edge detected SEM image for PMMA etched line space pattern obtained via LiNe flow. b) Histogram for LER for a). c) Comparison between experimental roughness and height averaged CGMD results. Yellow bars are from the experimental inhouse-image analysis method, green bars are from simulation, brown bars are the commercially used experimental image analysis method.

The deviations in line-edges obtained for each line in the SEM image is treated as a signal in length which is low-pass filtered to remove any spatial aliasing and subsequently windowed using a 4-term Blackman-Harris window to reduce emphasis on the edge points in the series. The cut-off frequency chosen was 0.9 times the Nyquist frequency. The processed signal is then Fourier transformed to generate a surface PSD of the 62 lines as shown in figure 9a. Beyond the correlation frequency, the high frequency contribution is further resolved by fitting a straight line for each of the 62 signals. The slope obtained from this fit denotes the fractal dimension, D (figure 9b) with $\langle D \rangle = 1.77 \pm 0.1016$. The fractal dimension for a self-similar series can be related to the Hurst or roughness exponent (H) by $D = 2 - H$, with higher H indicating a less volatile trend. $\langle H \rangle$ between 0 - 0.5 in general and $\langle H \rangle = 0.23$ for the current image signifies a long-term switching between high and low edge deviations in adjacent pixels lasting for a substantially long length across the line edge.

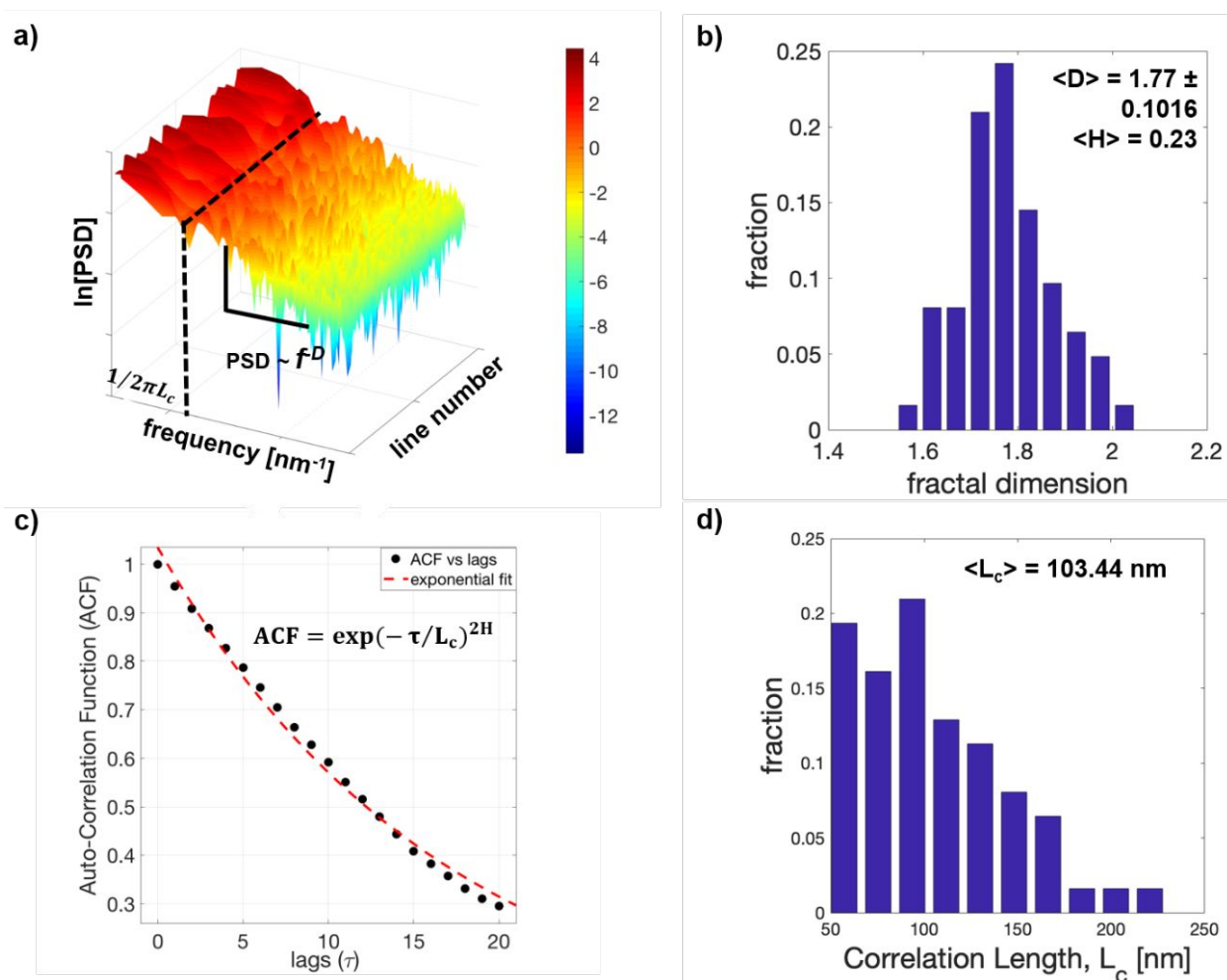


Figure 9. a) Surface power spectral density example plot. Beyond the correlation length, the PSD is fit to f - D . b) fractal dimension histogram for the 62 defect free lines captured through image analysis. c) exponential fit for the auto-correlation function for a sample line. The roughness exponent, H is obtained from figure 9b for each of the line. d) histogram for correlation length L_c , obtained from fitting the exponential auto-correlation function.

As figure 9a shows, the PSD for each of the individual line is noisy. The exact point of distinction between the low and high frequencies to obtain the correlation length can be tricky using only the PSD curves. Alternatively, the auto-correlation function (ACF) can be generated for each of the line as a function of the lags (τ). This ACF is fit to an exponential fall model, $\text{ACF} = \exp(-\tau/L_c)^{2H}$ as in figure 9c. The histogram for L_c is shown in figure 9d with $\langle L_c \rangle = 103.44$ nm indicating significant contribution from low frequency roughness. As we are limited with our simulation box

size with ~ 100 nm line length as opposed to 1500 nm for experimental line length, comparison in the frequency domains are not made for the two.

Finally, a 3D comparison of the dry etched simulation morphology with a cross-sectional PMMA etched SEM image was carried out. A qualitative comparison can be made between the experimental image in figure 10b with a simulation image of similar BCP blends both pre-etch and post-etch using selectivity = 3.5 in figure 10a. The cross-sectional image is processed to isolate individual domains and averaged out over the optimally detected PS domains. This edge detected averaged domain and one selected individual domain are compared with the pinned domain and the average of unpinned domain from the simulations. The results show that the experimental SEM images has a similar gradient trend for the line-width as compared to the dry-etching (figure 10c). This gradient is a closer matched for the pinned domain compared to the unpinned ones. Both pinned and unpinned areas showed a closer match with the selected experimental domain comparing to averaged experimental results. One of the reasons for the high averaged gradient in the SEM image could be a higher BCP mass at the bottom substrate. It is likely that the excess mass is caused by incomplete PMMA removal. Similar PS-PMMA phase densities lead to a poor interface distinction for the BCP edge. Correction for this overestimation will lead to a closer agreement. Moreover, in experiments, the film thickness is 35nm while in simulation it is 28nm. A higher thickness may lead to more gradient based on the trend shows in the SEM image.

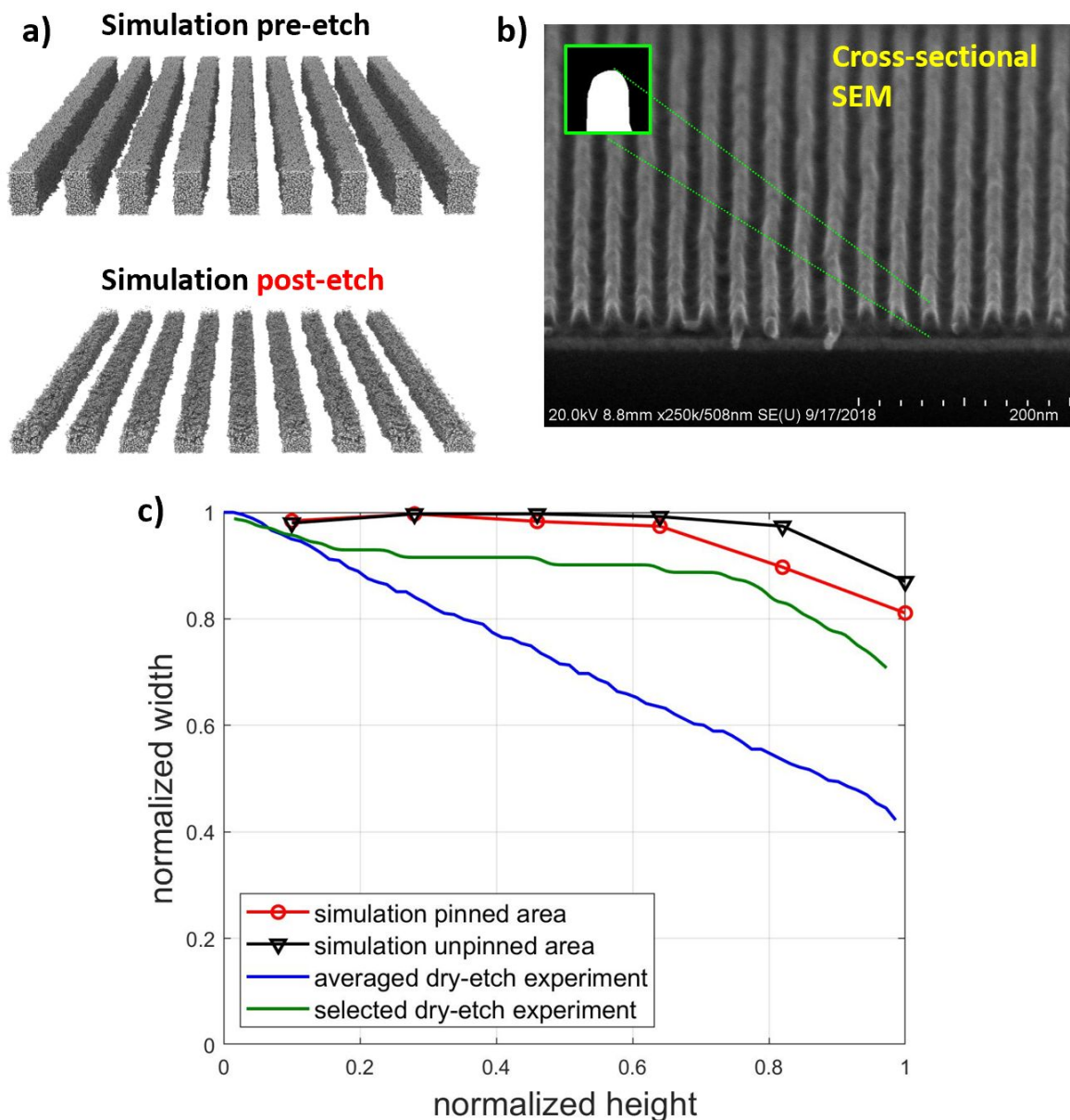


Figure 10. a) repeated patterns generated for the dry etched CGMD simulations on flat substrate geometry. b) cross-sectional SEM image for PMMA etched-off line and space patterns and one selected domain shape. c) remaining PS domain normalized line-width vs. normalized height for simulation pinned, unpinned areas and experimental averaged, selected areas.

IV. Conclusions

Using a large-scale CGMD model, we have studied the three-dimensional profiles of line and space patterns formed from symmetric BCPs at three process stages: anneal, pre-and post- dry etch. The etching is studied using a novel modeling approach for a DSA dry-etching schematic.

Etch gas selectivities were varied and the kinetic evolution with the instantaneous effective selectivity was assessed. For the optimized selectivity, the PS domain morphology was studied by evaluating the line-width and line edge roughness over the film thickness. Subsequently, a multi-stage roughness evaluation was performed at anneal, pre-etch and post-etch stages of the process. The roughness magnitude was the highest in the anneal stage followed by post-etch and pre-etch. This observation was also true on average in the frequency domain for both low and high frequencies.

Finally, comparison with equivalent Liu-Nealey flow experiments showed a close matching in the average roughness values obtained by processing the SEM images and the CGMD results. A similar gradient trend on the remaining PS domain after dry-etching was also observed in both simulation and experiments.

This work has introduced a novel etching simulation methodology in addition to the directed self-assembly of the BCP. Most of the prior DSA work essentially measured the pre-etch BCP interfacial-widths and not the post-etch edge roughness of the polymeric domains. The lower degree of coarse-graining also allows us to capture the high frequency roughness bands. The three-dimensional roughness analysis at various layer heights would give the experimentalist a better roughness estimate compared to an approximated value from SEM images. The reliance on sophisticated characterization like STEM tomography for accurate 3D roughness evaluation can also be reduced with aid from simulations similar to the ones described in the work. For the aforementioned reasons, this simulation model can be used as a time and resource saving tool to investigate and optimize process parameters like substrate dimensions, BCP properties, and etching parameters to form defect free lamellae with mitigated LER. The models lays a foundation to probe other problems of interest in DSA like the effect of substrate topography on 3D roughness or strategies to mitigate roughness with specific BCP blends.

The results on similar simulations for a topographical substrate will be shown in a subsequent publication. This model can be further improved by accounting for cross-linking of the PS surface upon interaction with the etch-beads and accounting for reactive-ion etching along with ion bombardment for the dry etching mechanism. Replacing the substrate stationary beads with hydroxy terminated PS-PMMA brush beads (same as in the experiments) might be another option to investigate the BCP-DSA and etch processes thoroughly.

Acknowledgments

The simulations were performed using LAMMPS open source software package.⁴⁰⁻⁴¹ The work was supported by EMD Performance Materials (Cornell OSP NO. 74981). This work used the Extreme Science and Engineering Discovery Environment (XSEDE)⁴², which is supported by National Science Foundation grant number ACI-1053575.

References

1. Jeong SJ, Kim JY, Kim BH, Moon HS, Kim SO. Directed self-assembly of block copolymers for next generation nanolithography. *Materials Today*. 2013 Dec 31;16(12):468-76.
2. Liu CC, Ramírez-Hernández A, Han E, Craig GS, Tada Y, Yoshida H, Kang H, Ji S, Gopalan P, de Pablo JJ, Nealey PF. Chemical patterns for directed self-assembly of lamellae-forming block copolymers with density multiplication of features. *Macromolecules*. 2013 Feb 11;46(4):1415-24.
3. Ruiz R, Kang H, Detcheverry FA, Dobisz E, Kercher DS, Albrecht TR, de Pablo JJ, Nealey PF. Density multiplication and improved lithography by directed block copolymer assembly. *Science*. 2008 Aug 15;321(5891):936-9.
4. Mack CA. *Field guide to optical lithography*. Bellingham, Washington, USA: SPIE Press; 2006 Jan 24.
5. Wu B, Kumar A. Extreme ultraviolet lithography: a review. *Journal of Vacuum Science & Technology B*. 2007 Nov 1;25(6):1743-61.
6. Bates FS, Fredrickson GH. Block copolymers-designer soft materials. *Physics today*. 2000.
7. Segalman RA, Schaefer KE, Fredrickson GH, Kramer EJ, Magonov S. Topographic templating of islands and holes in highly asymmetric block copolymer films. *Macromolecules*. 2003 Jun 17;36(12):4498-506.
8. KG AT, Gotrik KW, Hannon AF, Alexander-Katz A, Ross CA, Berggren KK. Templating three-dimensional self-assembled structures in bilayer block copolymer films. *Science*. 2012 Jun 8;336(6086):1294-8.
9. Pinge S, Lin G, Padmanaban M, Baskaran D, Joo YL. Designing an Ordered Template of Cylindrical Arrays based on a Simple Flat Plate Confinement of Block Copolymers: A Coarse-Grained Molecular Dynamics Study. *Soft Matter*. 2017. DOI: 10.1039/C7SM02015E.
10. Cheng JY, Rettner CT, Sanders DP, Kim HC, Hinsberg WD. Dense self-assembly on sparse chemical patterns: Rectifying and multiplying lithographic patterns using block copolymers. *Advanced Materials*. 2008 Aug 18;20(16):3155-8.

11. Kim SO, Solak HH, Stoykovich MP, Ferrier NJ, de Pablo JJ, Nealey PF. Epitaxial self-assembly of block copolymers on lithographically defined nanopatterned substrates. *Nature*. 2003 Jul 24;424(6947):411-4.
12. Liu CC, Han E, Onses MS, Thode CJ, Ji S, Gopalan P, Nealey PF. Fabrication of lithographically defined chemically patterned polymer brushes and mats. *Macromolecules*. 2011 Mar 18;44(7):1876-85.
13. Liu CC, Ramírez-Hernández A, Han E, Craig GS, Tada Y, Yoshida H, Kang H, Ji S, Gopalan P, de Pablo JJ, Nealey PF. Chemical patterns for directed self-assembly of lamellae-forming block copolymers with density multiplication of features. *Macromolecules*. 2013 Feb 11;46(4):1415-24.
14. Liu CC, Nealey PF, Ting YH, Wendt AE. Pattern transfer using poly (styrene-block-methyl methacrylate) copolymer films and reactive ion etching. *Journal of Vacuum Science & Technology B: Microelectronics and Nanometer Structures Processing, Measurement, and Phenomena*. 2007 Nov;25(6):1963-8.
15. Muramatsu M, Iwashita M, Kitano T, Toshima T, Somervell M, Seino Y, Kawamura D, Kanno M, Kobayashi K, Azuma T. Nanopatterning of diblock copolymer directed self-assembly lithography with wet development. *Journal of Micro/Nanolithography, MEMS, and MOEMS*. 2012 Jul 1;11(3):031305-1.
16. Black CT, Guarini KW, Milkove KR, Baker SM, Russell TP, Tuominen MT. Integration of self-assembled diblock copolymers for semiconductor capacitor fabrication. *Applied Physics Letters*. 2001 Jul 16;79(3):409-11.
17. Gharbi A, Tiron R, Pimenta Barros P, Argoud M, Servin I, Chevalier X, Nicolet C, Navarro C. PMMA removal options by wet development in PS-b-PMMA block copolymer for nanolithographic mask fabrication. *Journal of Vacuum Science & Technology B, Nanotechnology and Microelectronics: Materials, Processing, Measurement, and Phenomena*. 2015 Sep;33(5):051602.
18. Chung TY, Nest D, Graves DB, Weilnboeck F, Bruce RL, Oehrlein GS, Wang D, Li M, Hudson EA. Electron, ion and vacuum ultraviolet photon effects in 193 nm photoresist surface roughening. *Journal of physics D: Applied physics*. 2010 Jun 21;43(27):272001.

19. Nest D, Chung TY, Vegh JJ, Graves DB, Bruce RL, Lin T, Phaneuf RJ, Oehrlein GS, Long BK, Willson CG. Role of polymer structure and ceiling temperature in polymer roughening and degradation during plasma processing: a beam system study of P4MS and P α MS. *Journal of Physics D: Applied Physics*. 2010 Feb 12;43(8):085204.
20. Ting YH, Liu CC, Park SM, Jiang H, Nealey PF, Wendt AE. Surface roughening of polystyrene and poly (methyl methacrylate) in Ar/O₂ plasma etching. *Polymers*. 2010 Dec 2;2(4):649-63.
21. Zekonyte J, Zaporajtchenko V, Faupel F. Investigation of the drastic change in the sputter rate of polymers at low ion fluence. *Nuclear Instruments and Methods in Physics Research Section B: Beam Interactions with Materials and Atoms*. 2005 Jul 1;236(1-4):241-8.
22. Zaporajtchenko V, Zekonyte J, Faupel F. Effects of ion beam treatment on atomic and macroscopic adhesion of copper to different polymer materials. *Nuclear Instruments and Methods in Physics Research Section B: Beam Interactions with Materials and Atoms*. 2007 Dec 1;265(1):139-45.
23. Sumiya M, Bruce R, Engelmann S, Weilmboeck F, Oehrlein GS. Study of 193 nm photoresist degradation during short time fluorocarbon plasma exposure. I. Studies of modified layer formation. *Journal of Vacuum Science & Technology B: Microelectronics and Nanometer Structures Processing, Measurement, and Phenomena*. 2008 Sep;26(5):1637-46.
24. Sumiya M, Bruce R, Engelmann S, Weilmboeck F, Oehrlein GS. Study of 193 nm photoresist degradation during short time fluorocarbon plasma exposures. II. Plasma parameter trends for photoresist degradation. *Journal of Vacuum Science & Technology B: Microelectronics and Nanometer Structures Processing, Measurement, and Phenomena*. 2008 Sep;26(5):1647-53.
25. Baravelli E, Dixit A, Rooyackers R, Jurczak M, Speciale N, De Meyer K. Impact of line-edge roughness on FinFET matching performance. *IEEE Transactions on Electron Devices*. 2007 Sep;54(9):2466-74.
26. Leung G, Lai L, Gupta P, Chui CO. Device-and circuit-level variability caused by line edge roughness for sub-32-nm FinFET technologies. *IEEE Transactions on Electron Devices*. 2012 Aug;59(8):2057-63.

27. Bosse AW, Lin EK, Jones RL, Karim A. Interfacial fluctuations in an ideal block copolymer resist. *Soft Matter*. 2009;5(21):4266-71.
28. Matsen MW, Bates FS. Unifying weak-and strong-segregation block copolymer theories. *Macromolecules*. 1996 Feb 12;29(4):1091-8.
29. Detcheverry FA, Pike DQ, Nagpal U, Nealey PF, de Pablo JJ. Theoretically informed coarse grain simulations of block copolymer melts: method and applications. *Soft Matter*. 2009;5(24):4858-65.
30. Hur SM, Thapar V, Ramírez-Hernández A, Khaira G, Segal-Peretz T, Rincon-Delgadillo PA, Li W, Müller M, Nealey PF, de Pablo JJ. Molecular pathways for defect annihilation in directed self-assembly. *Proceedings of the National Academy of Sciences*. 2015 Nov 17;112(46):14144-9.
31. Hur SM, Khaira GS, Ramírez-Hernández A, Müller M, Nealey PF, de Pablo JJ. Simulation of defect reduction in block copolymer thin films by solvent annealing. *ACS Macro Letters*. 2014 Dec 11;4(1):11-5.
32. Daoulas KC, Müller M, Stoykovich MP, Kang H, de Pablo JJ, Nealey PF. Directed copolymer assembly on chemical substrate patterns: A phenomenological and single-chain-in-mean-field simulations study of the influence of roughness in the substrate pattern. *Langmuir*. 2008 Feb 19;24(4):1284-95.
33. Stoykovich MP, Daoulas KC, Müller M, Kang H, de Pablo JJ, Nealey PF. Remediation of line edge roughness in chemical nanopatterns by the directed assembly of overlying block copolymer films. *Macromolecules*. 2010 Feb 10;43(5):2334-42.
34. Segal-Peretz T, Ren J, Xiong S, Khaira G, Bowen A, Ocola LE, Divan R, Doxastakis M, Ferrier NJ, de Pablo J, Nealey PF. Quantitative three-dimensional characterization of block copolymer directed self-assembly on combined chemical and topographical prepatterned templates. *ACS nano*. 2017 Jan 17;11(2):1307-19.
35. Peters AJ, Lawson RA, Ludovice PJ, Henderson CL. Detailed molecular dynamics studies of block copolymer directed self-assembly: Effect of guiding layer properties. *Journal of Vacuum*

Science & Technology B, Nanotechnology and Microelectronics: Materials, Processing, Measurement, and Phenomena. 2013 Nov;31(6):06F302.

36. Peters AJ, Lawson RA, Ludovice PJ, Henderson CL. Effects of block copolymer polydispersity and χ_N on pattern line edge roughness and line width roughness from directed self-assembly of diblock copolymers. InProc SPIE 2013 Mar 26 (Vol. 8680, pp. 868020-1).

37. Morita H, Tanaka K, Kajiyama T, Nishi T, Doi M. Study of the glass transition temperature of polymer surface by coarse-grained molecular dynamics simulation. Macromolecules. 2006 Sep 5;39(18):6233-7.

38. Kremer K, Grest GS. Dynamics of entangled linear polymer melts: A molecular-dynamics simulation. The Journal of Chemical Physics. 1990 Apr 15;92(8):5057-86.

39. Weeks JD, Chandler D, Andersen HC. Role of repulsive forces in determining the equilibrium structure of simple liquids. The Journal of chemical physics. 1971 Jun 15;54(12):5237-47.

40. In't Veld PJ, Plimpton SJ, Grest GS. Accurate and efficient methods for modeling colloidal mixtures in an explicit solvent using molecular dynamics. Computer Physics Communications. 2008 Sep 1;179(5):320-9

41. Plimpton S. Fast parallel algorithms for short-range molecular dynamics. Journal of computational physics. 1995 Mar 1;117(1):1-9.

42. Towns J, Cockerill T, Dahan M, Foster I, Gaither K, Grimshaw A, Hazlewood V, Lathrop S, Lifka D, Peterson GD, Roskies R. XSEDE: accelerating scientific discovery. Computing in Science & Engineering. 2014 Sep 1;16(5):62-74.